Spring 2015

Computational study of nano- and meso-scale size effects on thermal transport

Eshaan Mathew
Purdue University

Graduate School Form 30
(Revised 08/14)

PURDUE UNIVERSITY
GRADUATE SCHOOL
Thesis/Dissertation Acceptance

This is to certify that the thesis/dissertation prepared

By Eshaan Mathew

Entitled
COMPUTATIONAL STUDY OF NANO- AND MESO-SCALE SIZE EFFECTS ON THERMAL TRANSPORT

For the degree of Master of Science in Mechanical Engineering

Is approved by the final examining committee:

Xiulin Ruan

Amy Marconnet

Ganesh Subbarayan

To the best of my knowledge and as understood by the student in the Thesis/Dissertation Agreement, Publication Delay, and Certification/Disclaimer (Graduate School Form 32), this thesis/dissertation adheres to the provisions of Purdue University's "Policy on Integrity in Research" and the use of copyrighted material.

Xiulin Ruan

Approved by Major Professor(s): _____

_____

Approved by: Ganesh Subbarayan 03/06/2015

Head of the Department Graduate Program Date

COMPUTATIONAL STUDY OF NANO- AND MESO-SCALE SIZE EFFECTS ON THERMAL TRANSPORT

A Thesis

Submitted to the Faculty

of

Purdue University

by

Eshaan Mathew

In Partial Fulfillment of the

Requirements for the Degree

of

Master of Science in Mechanical Engineering

May 2015

Purdue University

West Lafayette, Indiana

ACKNOWLEDGEMENTS

I would like to thank Prof. Xiulin Ruan for his patience and crucial insights, allowing me to take this project and make it successful. I also want to thank Dr. Ganesh Subbarayan and Dr. Amy Marconnet for their support on my committee.

My mentor Yan Wang, helped me grasp all the computational techniques used in this project, through every step and stage. I thank Tianli Feng, Ninad Trifale, Supriya Dharkar and Avneet Hira for sharing their perspectives about different aspects of the project

TABLE OF CONTENTS

Page

Page

LIST OF TABLES

Table Page

LIST OF FIGURES

Figure Page

Figure Page

Figure Page

NOMENCLATURE

Symbol	Units	Definition
a	m	Cell length
C	J/m^3K	Volumetric Heat Capacity
f	s^{-1}	Frequency of heat flux
G	W/m^3K	Electron to phonon energy transfer per unit volume or electron cooling rate
h	W/m^2K	Interfacial conductance
h_{ep}	W/m^2K	Electron-phonon conductance
h_{pp}	W/m^2K	Phonon-phonon conductance
J	W/m^2	Heat Flux
k	W/mK	Thermal Conductivity
k_B	1.38064E-23 m^2kg/s^2k	Boltzmann Constant
K_e	W/mK	Electron thermal conductivity

k_p	W/mK	Phonon thermal conductivity
$\bar{k}$	m^{-1}	Wave vector
L	m	Length of the system
L_p	m	Penetration depth
m	amu	Atomic mass
MF	Hz	Modulation frequency
n_b		Number of basis atoms
$\dot{q}$	W/m^3	Energy Generation term
t	s	Time
T	K	Temperature
T_e	K	Temperature of electron
T_p	K	Temperature of phonon
V_d		Volume fraction
X	m	Position, Distance

Greek

α	m^2/s	Thermal Diffusivity
ϕ	eV	Interaction Potential
ϵ	eV	Potential well depth
$\boldsymbol{\lambda}$	m	Mean Free Path
τ	s	Relaxation Time

σ	m	Zero potential energy pairwise separation
ν	m/s	Carrier Velocity
ω	rad/s	Applied modulation heat flux

ABSTRACT

Mathew Eshaan M.S.M.E., Purdue University, May 2015. Computational Study of Nano- and Meso-Scale Size Effects on Thermal Transport; Professor: Xiulin Ruan, School of Mechanical Engineering.

In the era where structures and devices are of the order of nanometers, a detailed understanding on the heat carriers in nanostructured devices is required to enable further improvements and advances.

In the first portion of this thesis we develop a new methodology to measure phonon mean free path (MFP) contribution to thermal conductivity. Molecular dynamics (MD) is used to determine the thermal conductivity of argon with a modified Leonard Jones potential as a function of the modulation frequency. We observe a decrease in the thermal conductivity as the heat transport enters the ballistic regime by an order of magnitude. This agrees with some of the recent literature on similar experimental work. We further compare the trends by performing Boltzmann Transport Equation (BTE) simulations.

In the second part we analyze the effective medium theory as modified by Minnich and Chen, to understand the size effect of metal particles in non-metal composites. We predict results for a range of materials and sizes, and compare the results using the two temperature model (TTM) and a finite element analysis.

CHAPTER 1. INTRODUCTION

1.1 Introduction

There is tremendous focus on research dealing with nanoscale energy transport - length scales equivalent to phonon mean free paths[1–5]. This is mainly owing to the fact that the effective properties of the materials and devices may be altered to show more desirable properties. With continual progress at micro and nano scale for fabrication processes and system integration, factors such as heat dissipation have made it difficult to improve the performance, efficiency and reliability of devices such as microprocessors and solar cells.

a) b)

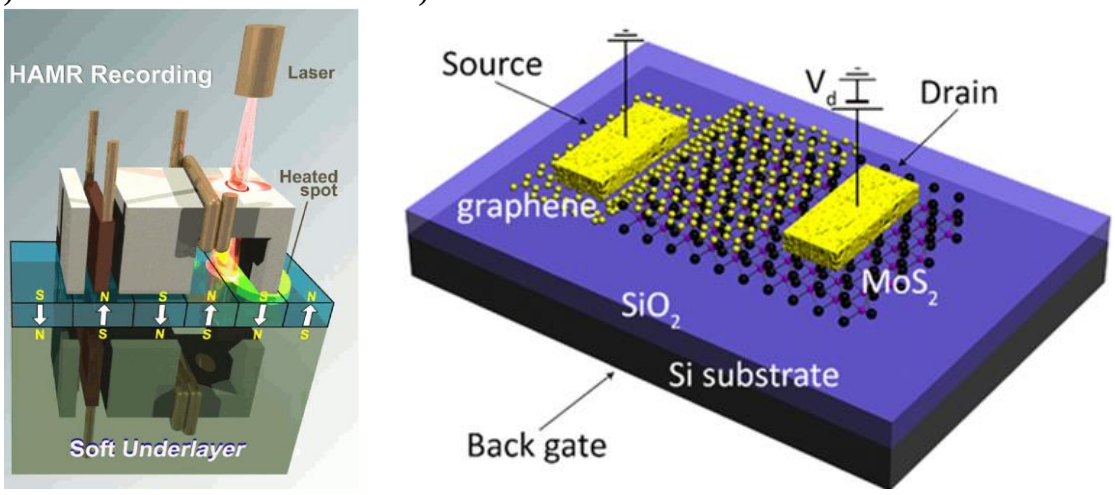

(D. Weller of Seagate Research)

Figure 1.1. a) Heat assisted magnetic recording device, b) Graphene MoS_2 based transistor[6].

To be able to alter material properties – create surface defects, modify grain boundaries or just fabricate nano-scale devices, it is imperative to have a clear understanding of heat transport mechanisms at the respective length scales. Figure 1.1 depicts a) a heat assisted magnetic recording device and b) a graphene-MoS_2 based transistor, both novel devices that need a better understanding of nano scale heat transfer to further evolve.

In this work, a detailed analysis of thermal transport involving nano/meso-scale effects is conducted. In the first portion, heat transfer under high modulating frequency is studied and a new technique is developed using MD and BTE simulations to predict the thermal conductivity for argon with a modified LJ potential. The resulting nonlocal effects caused by the fast switching transients is evaluated and compared with the bulk properties of the material.

The second portion of this thesis deals with electron-phonon coupled thermal transport in composite materials with micro- to nano-sized inclusions. The effective thermal conductivity of the material as a function of the inclusion size is investigated. Further, a critical size inclusion is calculated that would result in the particle ceasing to exhibit any effective thermal effect on the composite

CHAPTER 2. BALLISTIC TRANSPORT IN HIGH FREQUENCY FLUX DOMAIN

2.1 Theory and Significance of Ballistic Transport

2.1.1 Heat Transfer via Conduction in Solids

The Fourier's Law comes into effect for large length scales via conduction in solids. The thermal conductivity of a solid in one dimension may be computed by the following equation[7,8]

$$k = -J\frac{dx}{dT} \tag{2.1}$$

where k is thermal conductivity, J is the heat flux, over distance x and T is the temperature. This is dependent on the material properties and temperature difference across measured ends thus making it a local theory [9]. The other considerations while solving using this temperature profile is that the system of interest behaves classically and the energy transport is diffusive.

2.1.2 Ballistic Energy Transport

In semiconductors or insulators, the collective lattice vibrations or phonons account for the dominant portion of the heat conduction. At length scales comparable to the mean free paths (MFP) of phonons, the classical heat conduction models based on Fourier's law fail as the regime fails to attain local thermal equilibrium resulting in non-diffusive/ballistic transport. The heat transport properties of the material/device change from that of the bulk

values. Phonons in non-metals have a range of frequencies and mean free paths, thus the energy transport transits from diffusive to ballistic gradually, with the Fourier's law being less accurate for smaller length scales[4,10].

Another equation to approximately predict the thermal conductivity is via kinetic theory [11] which is used to derive thermos-physical properties of a broad range of materials. It considers the particles as separate entities that collide and scatter with each other and with boundaries.

$$k = \frac{1}{3} C\, v \lambda_{avg} \qquad 2.2$$

Where C is the volumetric heat capacity, ν is the carrier velocity and λ_{avg} is the average distance travelled by the carriers between collisions - mean free path. It is considered that a particle travels in a given direction over a length λ, after which it collides and causes heat flux as a function of the velocity and MFP of the particle. This gray technique using mean free paths of carriers works well in gases but again fails to predict the thermal conductivity in solids that have a large spectrum of mean free paths for phonons[12].
To segregate the thermal conductivity relating to the mean free path of the phonons the accumulation function is given by[13]

$$k_{acc} = \sum_{s} \int_{0}^{\lambda^*} \frac{1}{3} C_{MFP}(\lambda) v(\lambda) \lambda d\lambda \qquad 2.3$$

Where λ is the phonon MFP, C_{MFP} is the volumetric heat capacity per unit phonon MFP and s indexes the phonon polarization. Thus Equation (2.3) helps determine the accumulated thermal conductivity contribution of phonons with MFPs less than or equal

λ^*. This particular equation is of great interest owing to the fact that it helps predict the thermal properties of nanostructures that fail to achieve the bulk thermal conductivity.

2.1.3 Frequency Dependence of Thermal Conductivity

Several studies have shown the dependence of frequency on the thermal conductivity of given materials using several experimental and numerical techniques[9,12,14,15]. The periodic heat flux induced by the pump laser results in a thermal response with a characteristic penetration depth.

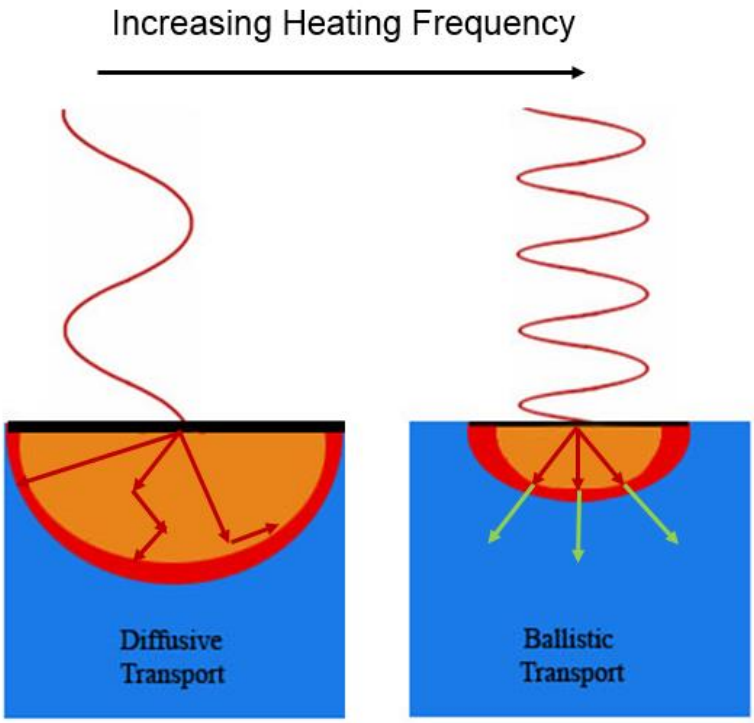

Figure 2.1. Depiction of change in thermal penetration depth of phonons as a function of input modulation frequency.

As depicted in figure 2.1, an increasing heating frequency results in a decrease in the characteristic penetration depth given by the Equation (2.4) hypothesized by Koh and Cahill[14]

$$L_p = \sqrt{\frac{k}{C\pi f}} \tag{2.4}$$

where L_p is the penetration depth, k is the thermal conductivity, C is the volumetric heat capacity and f is the modulation frequency of the input flux. Equation (2.4) helps determine the thermal penetration depth, which implies that phonons with MFP>L_p will travel ballistically.

As per the experimental setups in several groups the specimen is considered as a semi-infinite solid with periodic heating boundary condition at one end. The frequency and value of the applied heat flux are the known parameters and the surface temperature rise can be measured. The fluctuation amplitudes decays exponentially from the temperature rise at the surface of the substrate. To derive the thermal conductivity based on the surface temperature rise of the substrate, by applying Fourier's law at x= 0 we obtain Equation (2.5) [8]

$$J = k\,\Delta T\sqrt{\frac{\omega}{\alpha}}\sin(\acute{\omega}t + \frac{\pi}{4}) \tag{2.5}$$

where ω is the modulation frequency ($2\pi f$) of the applied flux and α is the thermal diffusivity.

As depicted in figure 2.2 the temperature within the system fluctuates about the mean temperature T_i as a result of the input modulation heat flux at the surface. The temperature profile as a given angular frequency may be computed as

$$T(0,t) = T_i + \Delta T \sin \omega t \qquad 2.6$$

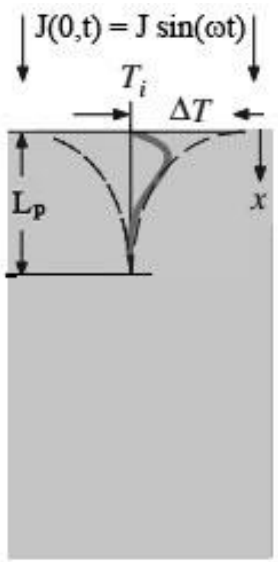

Figure 2.2. Semi-infinite device with applied high frequency heat flux resulting in a penetration depth.

The temperature rise of the interior point nodes of the system may be fitted to predict the apparent thermal conductivity from the ratio of the temperature rise at interior points and the surface at any time t as

$$\frac{T(x,t) - T_i}{\Delta T} = \exp\left[-x\sqrt{\frac{\omega}{2\alpha}}\right] \qquad 2.7$$

This solution may only be applied after a quasi-steady state has been achieved in the system at which the temperature profile through the system fluctuates steadily across the average temperature value of the system.

2.1.4 Experimental Techniques and Progress

Several groups have been trying to induce non-diffusive thermal transport and experimentally measure the k_{acc} by modifying the length scales of heat transport in the

regime of phonon MFPs. Time domain thermoreflectance(TDTR) technique has emerged as an important tool to measure thermal conductivity with the possibility for application over a range of sample geometries and dimensions[2,4,12,14,16]. It is an optical non contact method that can be applied in high temperature microscope settings. Here the length scale of the experiment corresponds to the spot size of the laser. The limitation of this technique is that it requires the surface of the sample to be extremely smooth, ideally under 15nm [2]. The technique is sensitive to the thermal conductivity in the through thickness direction, the direction anti parallel to surface normal. Also, the techniques applicability at low temperatures<30K is limited. Broadband frequency domain thermoreflectance (BB-FDTR) is another technique that takes the penetration depth as the main length scale. The use of continuous wave lasers in this technique help eliminate multiple time scales associated with TDTR [12,15]. BB-FDTR does not allow for measurements in the nanosecond regime which is possible in the TDTR experiments. Transient Thermal Grating (TTG) is another technique that is used where in the period of the pulsed optical grating is in the scale of the MFP of the phonons and a periodic temperature profile is subsequently induced[17,18].

Koh et al. use TDTR to measure MFPs of $In_{0.49}Ga_{0.51}P_{0.53}$, $In_{0.53}Ga0._{47}As$ and $Si_{0.4}Ge_{0.6}$ as a function of modulation frequency and limited by the same. They assume some of the phonons to be ballistic over the cross plane thermal diffusion length[14]. They conduct their experiments over a range of modulation frequencies, 0.1 to 10MHz and temperature 88 to 300K. They provide evidence of the dependence of thermal conductivity on frequency in their epitaxial semiconductor alloys. Chen et al. developed one of the first experimental technique that measures MFPs of phonons for thermal conduction. This

thermal conductivity spectroscopy technique was applicable across a wide range of materials and length scales, giving direct insight into distribution of heat across different phonon modes[18]. The thermal conductivity measure by them was independent of modulation frequency, with the pump diameter being the dominant length in contrast to the 1-dimensional thermal penetration depth.

Malen et al. use BB-FDTR technique to probe into the thermal conductivity of GaAs, GaN, AlN and 4H-SiC as a function of the phonon MFP, by generating a high frequency surface temperature modulation to produce non-diffusive phonon transport[12]. To be able to develop a better expression for the universal thermal conductivity accumulation function at high temperatures, they take into consideration the dominance of Umklapp scattering at temperatures above peak thermal conductivity. They thus take the expression for relaxation time as [19]

$$\tau^{-1} = Pe_v^{-\frac{C_U}{T}} T\omega^2 \qquad 2.8$$

Here τ is the relaxation time, P and C_U represent material constants that describe the Umklapp scattering rates, T is the temperature and ω is the phonon frequency. In another paper, Malen et al. also estimate the span of phonon MFP contributions in silicon over 0.3-8 μm. They conclude that MFP in the micron range contribute to the thermal conductivity and show that samples with a smaller L_P show reduced thermal conductivity.

2.2 Current Techniques to Predict k_{bulk}

2.2.1 Non-Equilibrium Molecular Dynamics (NEMD)

2.2.1.1 A Brief Introduction to NEMD

Molecular Dynamics is an atomic level method that integrates Newton's second law of motion restricted to follow classical dynamics. The interatomic potential determines the applied forces between the atoms[20,21]. MD simulations naturally take into account structural details such as defects, interface, strain, surface reconstruction, etc[22].

For thermal transport modelling MD is limited by the following drawbacks. In many systems the computational requirements to obtain enough data to observe forming trends for the technique are massive. MD cannot also explicitly include electrons. Also, since the calculation mechanism is classical the phonon mode energy is taken as k_bT and the actual energy distribution given by plank distribution is not taken into account.

NEMD technique is commonly used to predict the k_{bulk} of given materials. A temperature gradient across the simulation cell is maintained by applying temperature boundary conditions at the two ends. This in turn generates a heat current across the system. We may then calculate the thermal conductivity using Fourier's law from Equation (2.1).

Where A is the cross sectional area of the system. The phonon MFP due to scattering of phonons at the boundaries is limited by the Equation (2.9)

$$\lambda^{-1} = \lambda_{\infty}^{-1} + L^{-1} \qquad 2.9$$

Where λ is the phonon MFP, $\lambda\infty$ is the intrinsic phonon MFP in the bulk limit and L is the distance between the thermostats[23]. In the given technique a heat source and a heat sink are designed on the sides of the simulation domain creating a temperature gradient. Using

Fourier's law the gradient at steady state is used to predict the thermal conductivity of the system[2].

2.2.1.2 Model System and Simulation Results

The unitary model system composed of atoms having an atomic mass of 40.0g/mol was constructed by stacking face centered cubic unit cells in the [1 0 0] direction. The total length of the system was 600 nm with a cross sectional area of 456 sq. Å. The Lennard-Jones (LJ) potential was used to model the interatomic interactions using the Equation (2.10)

$$\varphi_{ri}(r_{ij}) = 4\epsilon[\left(\frac{\sigma}{r_{ij}}\right)^{12} - \left(\frac{\sigma}{r_{ij}}\right)^{6}] \qquad 2.10$$

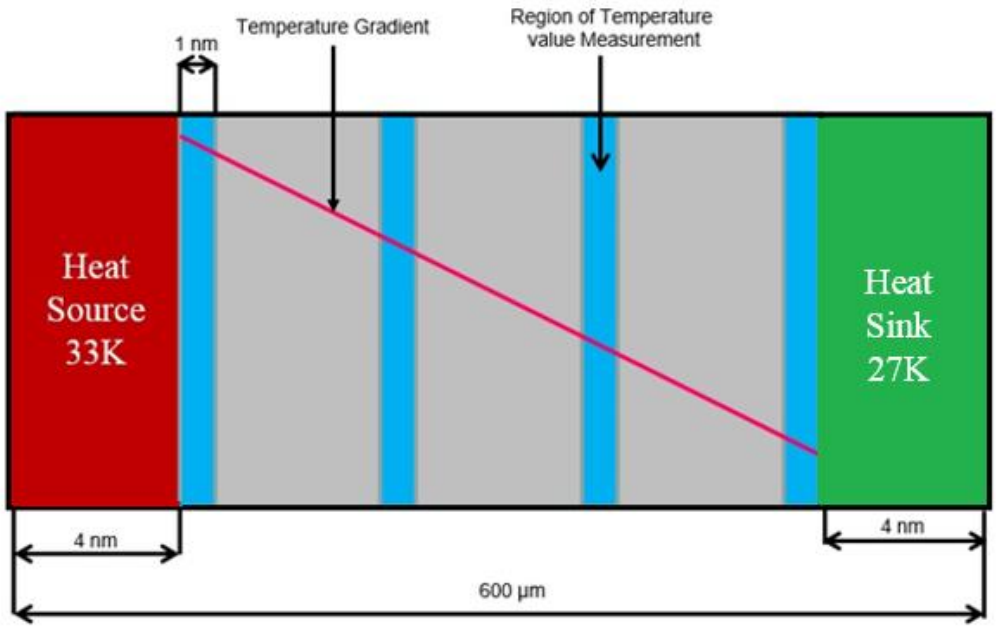

Figure 2.3. Schematic for device with heat bath and heat sink used to perform NEMD simulations.

Where φ_{ij} is pairwise interaction potential , r_{ij} is the distance between atoms i and j, σ is the zero potential energy pair separation and ϵ is the potential well depth. As compared to the parameters for a general argon structure σ_{Ar}= 0.34 nm, ϵ_{Ar}=0.0104 eV, the modification for the current system consisted of a cutoff radius of 2.5 σ_{Ar} and $\epsilon = 16\epsilon_{Ar}$ thus creating an overall bonding potential much stronger than found in argon. The temperature ws maintained at 30 K. This was done in order for the structure to mimic materials like Si, Ge. This is done because running these simulations on silicon are computationally expensive. The argon substrate can help accurately predict the trend and material properties while being computationally less demanding.

We leave out 1 nm regions at the two ends of the system (dark regions) as frozen to serve as fixed boundary conditions. The device of length 400nm is sandwiched between heat baths on either end of length 100nm each. Simulation time step used over here is 1fs based on criteria [24]

$$\Delta t = 0.002\sqrt{\frac{\sigma^2 m}{\epsilon}} \qquad 2.11$$

The simulations are used using LAMMPS package. Periodic boundary conditions are applied to all three directions with x as the length direction [100] and y and z as the lateral directions. Gaussian distribution is used to assign each atom with a random velocity vector, having a total mean of 0 and temperature variance of 5 K. The domain is relaxed to a NPT ensemble with a 0 pressure. Over a duration of 100 ps the temperature of the system is raised gradually to 30K and then maintained at that temperature for another 100 ps. The NEMD simulation consists of the heat baths the left one acting as a heat source while the one on the right acts as a heat sink. Input and output flux is applied with a magnitude of

0.025eV/ps. The simulation is run for a period of 20ns to enable the temperature of the system to reach steady state. The temperature gradient observed is 32.9K and 27.4K on the T_L and T_R. The thermal conductivity of the system is then calculated using

$$k = L\frac{J}{A(T_L - T_R)} \qquad 2.12$$

The figure 6 depicts the temperature gradient observed from the simulation. Solving gives us a bulk thermal conductivity of 97 W/mK.

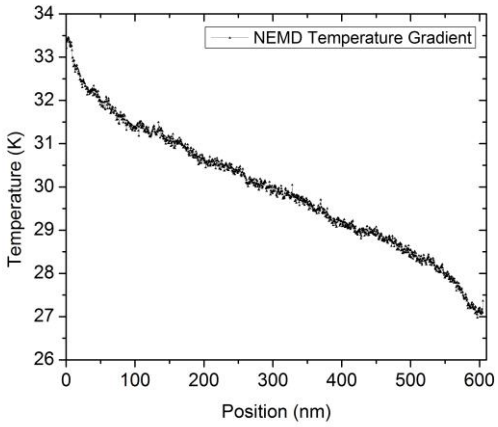

Figure 2.4. Temperature Gradient across the system obtained via NEMD simulations.

2.2.2 Green Kubo Method (GK)

2.2.2.1 A Brief Introduction to GK

Using MD simulations Green Kubo technique[25] is one of the approaches used to predict the bulk thermal conductivity of system. Green Kubo method thermal conductivity is determined based on the time it takes for the heat current fluctuations in the solid to dissipate. Several groups have persistently used the Green Kubo approach to estimate the thermal conductivity of an array of materials like silicon, graphene, Bi_2TE_3 and argon[26–30]. The k for a given direction can be calculated using the formula[7]

$$k_i = \frac{1}{k_b V T^2} \int_0^\infty J_i(t) J_i(0) dt \qquad 2.13$$

Where the subscript i denotes the direction in which the property is measured, V is the volume of the simulation cell, k_B is the Boltzmann constant, T is the temperature, t is the timestep and the $J_i(t)J_i(0)$ denote the autocorrelation function. In materials where the fluctuations are long lived the autocorrelation function dies slowly and requires a large simulation domain in the direction of the temperature gradient to accurately predict the thermal conductivity value and eliminate any size effect. Whereas in amorphous materials the thermal fluctuations quickly dampen as the MFP of the phonon is small[29].

2.2.2.2 Model System and Simulation Results

The same unitary model is used as NEMD with simulation performed in the [1 0 0] direction but with a length of 1.6μm and 456 sq. Å. The reason the length is changed over the two simulations is because NEMD can provide results over a smaller domain as compared to GK for the given material. Thus optimizing the domain size helps reduce computational costs for certain simulations. The LJ potential is again modified to mimic

Si. We again leave out 1 nm regions at the two ends of the system (dark regions) as frozen to serve as fixed boundary conditions for the MD simulation in LAMMPS. Periodic boundary conditions are applied to all three directions with x as the length direction [100] and y and z as the lateral directions. Gaussian distribution is used to assign each atom with a random velocity vector, having a total mean of 0 and temperature variance of 5 K. The domain is relaxed to a NPT ensemble with a 0 pressure. Over a duration of 100 ps the temperature of the system is raised gradually to 30K and then maintained for another 100 ps. Over a period of 12 ns the directional flux vectors are obtained and the GK simulation is run for 1.5 ns.

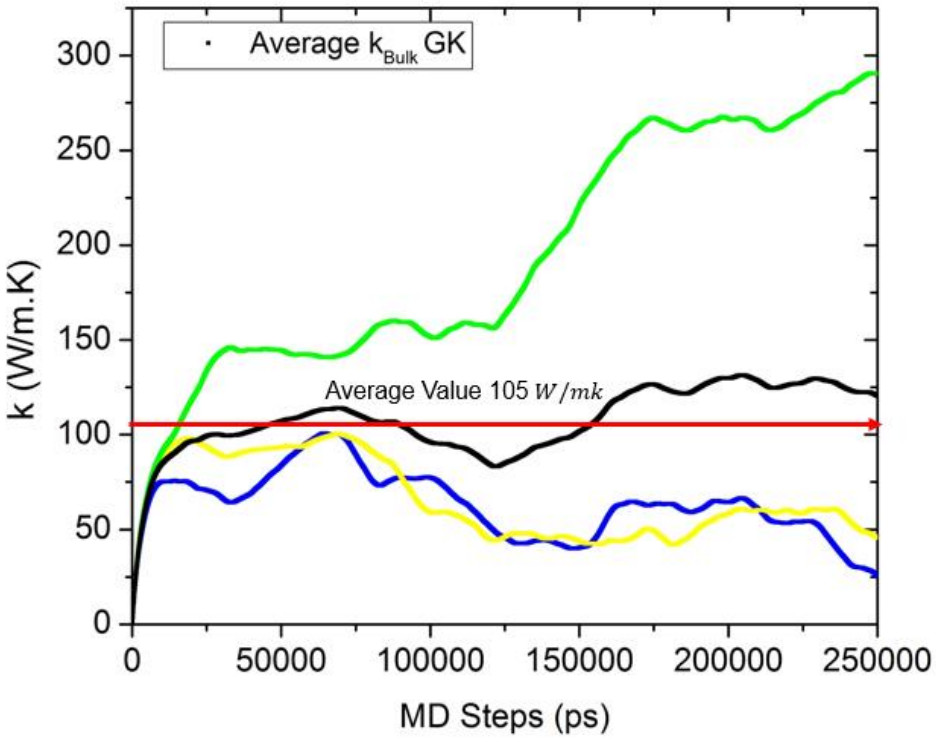

Figure 2.5. k_{Bulk} from Green Kubo Method using directional average.

The results from the NEMD simulation is depicted in figure 2.5. The average thermal conductivity values in the x, y and z direction are approximated from 6 simulations with a bulk value of 105 ± 12 W/mK.

2.2.3 Spectral Energy Density Method (SED)

2.2.3.1 A Brief Introduction to SED

We probe into the spectral properties of individual phonon modes through spectral density analysis. In contrast to the GK technique which provides only the bulk thermal conductivity of the given material, the SED approach helps predict the impact of the phonon modes in their contribution to thermal conductivity based on their MFPs[27,31,32]. Based on the velocities of the atoms the SED function is as given

$$\psi(k,\omega) = \sum_{\alpha}^{3} \sum_{b}^{n_b} \frac{m_b}{4\pi\tau_0 N_T} \left[\int_0^{t_0} U_\alpha^{b,l}(t) \,.\, \exp\left[i\bar{k}.r_0^l - i\omega t\right] dt \right]^2 \qquad 2.14$$

Where $U_\alpha^{b,l}$ represents the alpha component of the velocity of basis atom b in cell l, $\bar{k}$ represents the wave vector, ω is the angular frequency, t_0 is the integration time constant, α represents the x,y,z directions, b is the index of the basis atom, n_b is the number of basis atoms, l is the index of cells, N_t is the total number of cells, m_b represents the atomic mass of the basis atom b and r_0^l is the position coordinates of the atoms.

Using MD simulations in the LAMMPS package we obtain the time dependent velocity trajectories of the atoms. By defining the wave vectors, the relaxation time can be inferred by fitting the SED function to

$$\psi(\bar{k},\omega) = \sum_{v}^{2n_b} \frac{C(\bar{k},i)}{\left[2\tau\left(\omega - \omega_0(\bar{k},i)\right)\right]^2 + 1} \qquad 2.15$$

Where i is the index of phonon branches and C ($\bar{k}$, ν) is the combined coefficients as weighing factors for Lorentzian functions and τ fully-anharmonic phonon relaxation time.

2.2.3.2 Model System and Simulation Results

With the same bonding parameters a 8X8X8 system with 2048 atoms is constructed. The temperature is chosen at 30 K for comparative results with the other simulations. Due to requirement for periodicity, the $\bar{k}$ vectors only from the first brillouin zone for a unit cell are taken into consideration. In the direction [1 0 0], 9 $\bar{k}$ points were chosen to represent the center to the edge of the brillouin zone. By fitting the SED peaks corresponding to each of the wave vectors with the Equation (2.16) we are able to procure the relaxation times of the phonons as a function of the frequency of the phonons.

a)

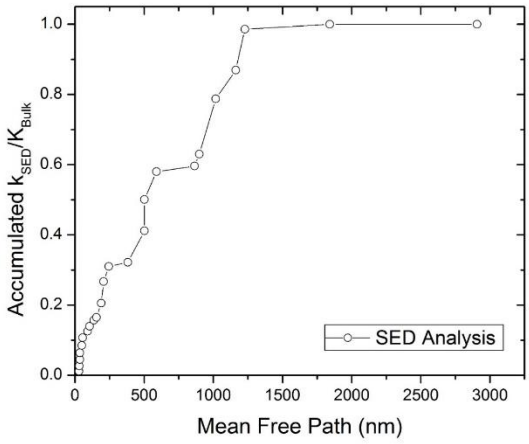

Figure 2.6. a) SED derived thermal conductivity as a function of the normalized phonon MFP. b) Dispersion relation that helps determine the phonon average velocity at a given wave vector. c) Example of an SED derived from the dispersion curve.

b) c)

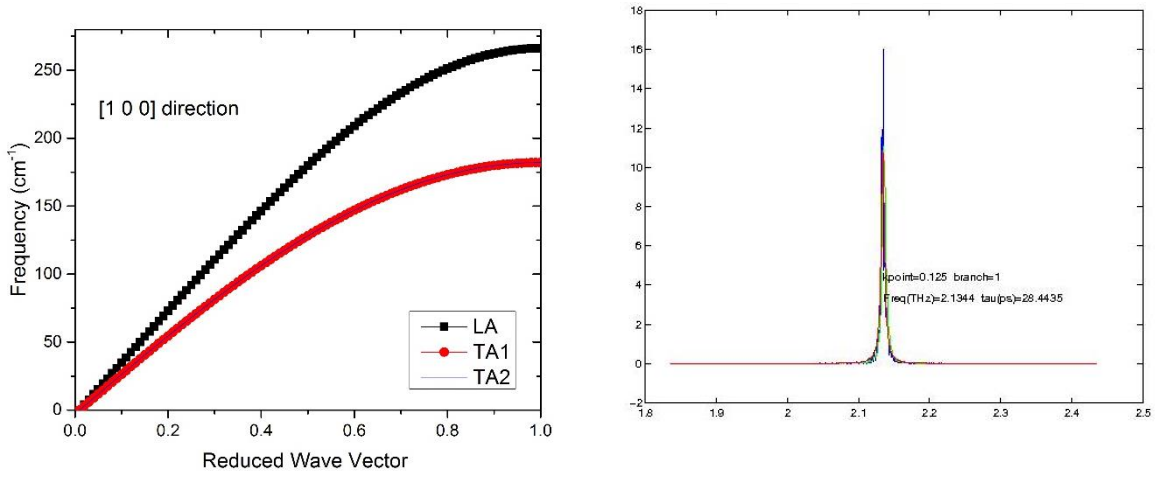

Figure 2.6. Continued.

The figure 2.6.a shows the thermal conductivity contribution of the phonons with the normalized k fitted against the phonon MFP. The results suggest that 50% of the thermal conductivity is contributed by phonons of MFPs less than 500nm whereas the system attains bulk thermal conductivity at about 1750nm. This implies that systems and devices with harbor phonon MFPs less than 1750nm for the given material would not be able to achieve bulk thermal conductivity. We also use GULP to include lattice dynamics calculations [33]. The dispersion relation in figure 2.6.b helps determine the phonon average velocity for a given wave vector by calculating the slope at that point. An example of the peaks obtained for the SED calculation is given in figure 2.6.c from one of the TA branches. The full width at the half max (FWHM) of the peak helps obtain the half of the inverse of the relaxation time. This value may be fitted to the kinetic theory to obtain the thermal conductivity for the given wave vector.

2.3 Modulation Frequency Dependent Thermal Conductivity Predictions

2.3.1 Modulation Frequency MD (MFMD)

2.3.1.1 Model System

The unitary model system composed of m40 atoms having an atomic mass of 40.0g/mol was constructed by stacking face centered cubic unit cells in the [100] direction. The total length of the system in the x direction is 1.6 μm and cross sectional area 456 sq. Å. The same parameters with a stronger LJ potential was used to model the interatomic interactions. The schematic in 2.7 shows the structure used to determine the temperature profile at the surface at within the device.

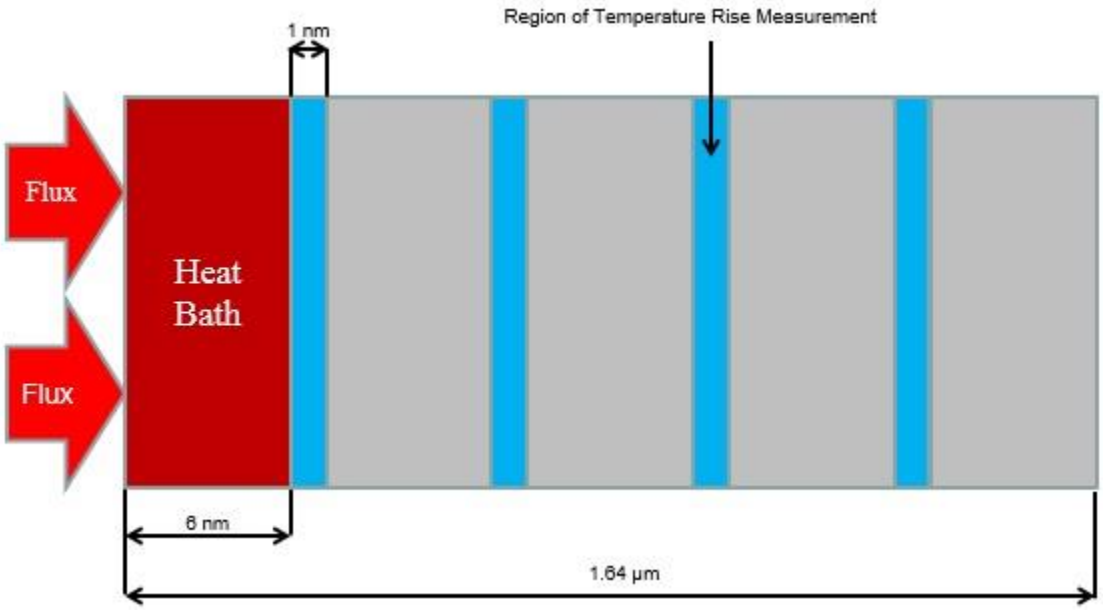

Figure 2.7. Schematic for modulation temperature MFMD simulation system.

2.3.1.2 Simulation Parameters and Results

The simulation time step used is the same as in the previous case at 1fs. The simulations are performed using LAMMPS package. Periodic boundary conditions are applied in the y and z lateral directions with x as the length direction [100]. Gaussian distribution is used to assign each atom with a random velocity vector, having a total mean of 0 and temperature variance of 5 K. The domain is relaxed to a NPT ensemble with a 0 pressure. Over a duration of 100 ps the temperature of the system is raised gradually to 30K and then maintained for another 100 ps.

The heat bath is designed at the left end of the device. The heat bath exists from 1nm to 6nm on the left end. The device extends from 7nm till 1.6 μm. 1nm bins are designated over the system to extract the temperature profile at the surface – 7nm from the left end and at several interior points in the system. The assigned temperature profile extraction bins are equally spaced from the device surface. The distance varies based on the modulated heat flux applied at the surface so as to have 6-10 bins at a length scale less than the penetration depth.

The heat flux applied in the heat bath is a sinusoidal wave with an amplitude varying again with the frequency of heat flux being studied. Ideally high frequency fluxes are given a higher amplitude to account for the short time period they peak amplitude for. The simulation with a nodulation frequency (MF) 500MHz is run for a time period of 150ns while the frequency 1THz is run for a period of 2ns. This helps account for ten input heat flux waves that ensure quasi-static state in the system.

a)

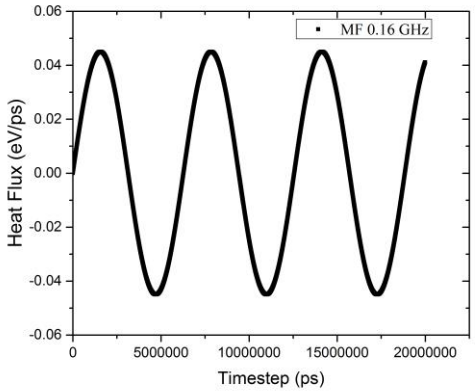

b)

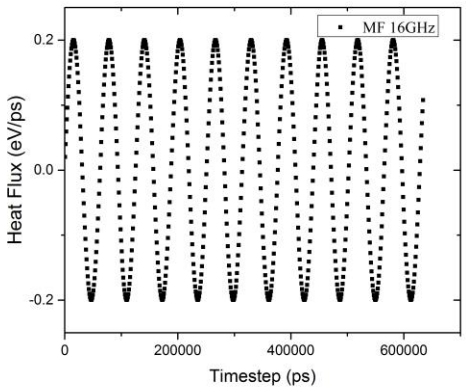

c)

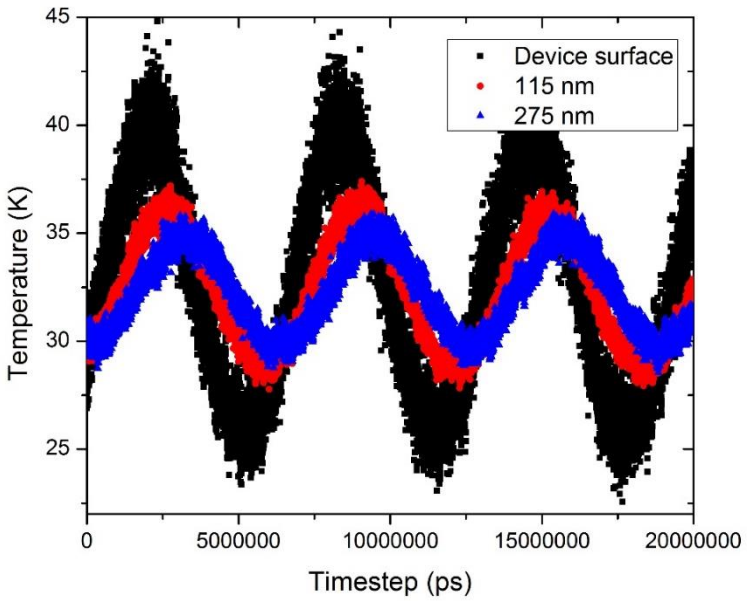

Figure 2.8. a) An example of input heat flux for MF 0.16GHz, b) MF 16GHz, c) Change in temperature amplitude from the surface to interior points as a result of temperature decay for MF of 0.16GHz.

Simulations were run for frequencies 79MHz, 0.16GHz, 0.79GHx, 1.6GHz, 7.9GHz, 16GHz, 79GHz and 0.16THz. All the parameters except the amplitude of the input heat flux were kept constant. In most cases the heat flux was varied with the frequencies to keep

a check on the surface temperature amplitude obtained. The heat flux was increased with increase in frequency. There is a difference of two orders of magnitude between the two. In a hypothetical case with the heat flux being the same for the two studies, if the heat flux in both the devices were to be that of the 0.16GHz case the 16GHz would have had a negligible temperature rise. Figure 2.8.c depicts the temperature amplitude at different positions within the device for an applied surface heat modulation of 0.16GHz. The temperature decay as discussed previously is exponential within the device. The black, red and blue curves depict the temperature at the device surface – 0nm, 115 nm from the heat bath and 275 nm from the heat bath as a function of time, respectively. The positions for heat extraction within the device were decided by dividing the theoretical penetration depth from Equation (2.4) and dividing it into ten approximate parts 1 nm wide. This was decided because the temperature amplitude till the penetration depth decays to a point where it is comparable to the internal fluctuations within MD and the data extracted would be unreliable. Using fast Fourier transform the peaks of the harmonic temperature waves was extracted in MATLAB.

Two different techniques were used here to fit the data and arrive at an apparent thermal conductivity for the system. First, using Equation (2.5), the temperature rise at the surface of the device was used to fit the k. This approach requires knowledge of the frequency and amplitude of the input flux, temperature rise at the surface of the device and the heat capacity of the material. This then solves back for the thermal conductivity as a function of the applied frequency. This approach replicates the technique and methodology used in experimental setups. As in most experiments with control of the input flux frequency and

magnitude, the surface temperature rise is the most accessible parameter that one can measure. This method using only the surface temperature data is termed as $MFMD_{Surf}$.

The second technique makes use of the temperature rise at the surface as well as the region underneath. Using Equation (2.7) we fit the temperature rise in the device to an exponential decay curve to obtain α. This method making use of temperature data points at the surface and at interior points is termed as $MFMD_{Int}$.

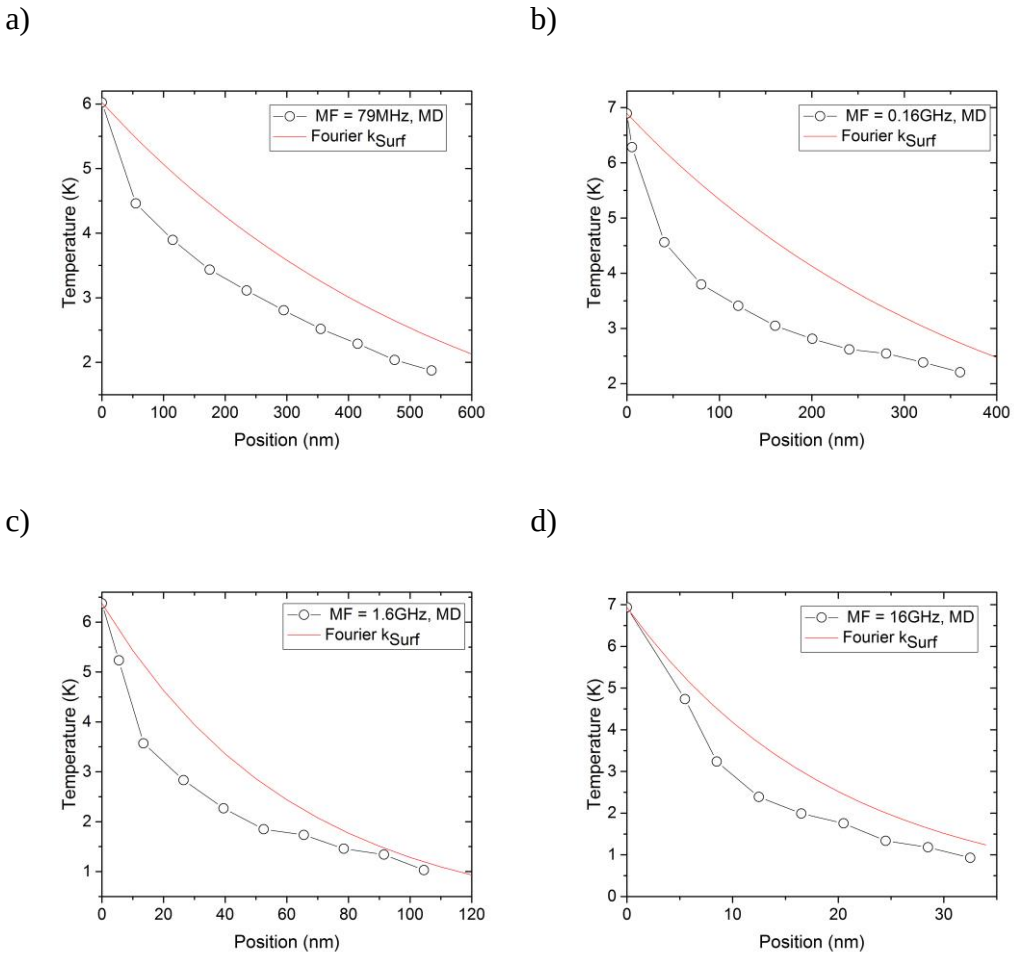

Figure 2.9. Magnitude of the local temperature oscillation as a function of position obtained from the MFMD simulations fitted with the Fourier's law for a)79MHz, b)0.16GHz, c)1.6GHz, d)16GHz.

2.3.1.3 Convergence Study

Two types of convergence test were conducted to ensure that our simulation results accurately reflect the intrinsic properties of the system. We first vary the magnitude of applied heat flux and then we vary the size of the heat bath. We then compare the surface temperature and overall trend of temperature decay at interior points in the device.

a)

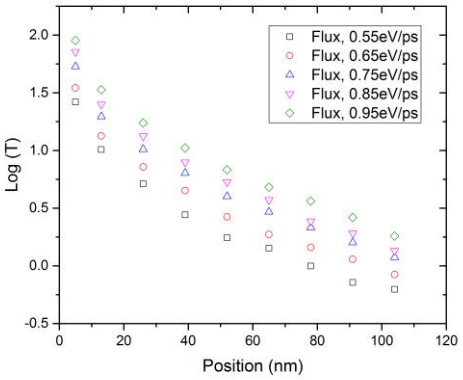

b)

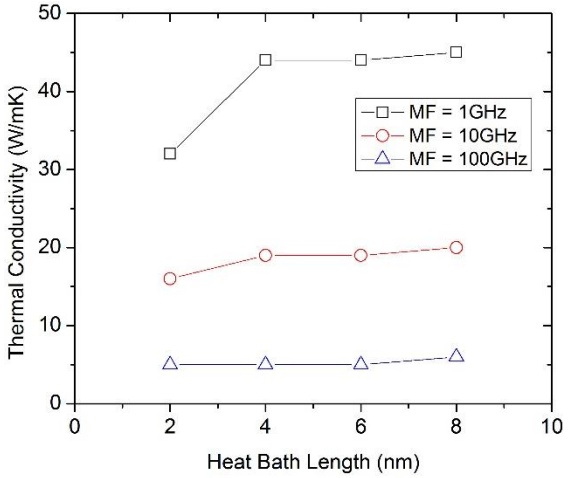

Figure 2.10. a) Studying Temperature drop as a function of change in flux magnitude for MF 1.6GHz, b) Convergence study for change inmeasure thermal conductivity via MFMD for change in heat bath length.

Figure 2.10.a depicts a case for MF 1.6GHz and shows the trend of the heat flux drop within the system. The y axis is logarithmic temperature rise and the temperature drop for different fluxes seems to show the same trend. The measured final values of the thermal conductivity are also in the range of ± 5 W/mK. It can be inferred that as long as the harmonic temperature magnitude remain positive, any change in the magnitude of the heat flux will not have a significant effect on the simulation. From figure 2.10.b it is observed that a small heat bath size may in some cases affects the measured value of the thermal conductivity. But convergence was observed for heat bath sizes ranging upwards from 4nm. Thus in all the MFMD simulations a heat bath size of 6nm was used.

2.3.2 Transient Boltzmann Transport Equation (MFBTE)

2.3.2.1 Brief Introduction to BTE

Boltzmann transport equation (BTE) is another technique to solve for thermal transport in solids, with the equations forms and scattering mechanisms well known for electrons and phonons [34]. This method can explain the dependence of thermal conductivity on temperature, quantum confinement, isotope scattering and distribution of impurities.

Malen et al. developed an analytical BTE solution to non-diffusive phonon thermal conductivity accumulation measurements for thermoreflectance technique. They took into account the thermal resistance arising from the interactions between the surface and the ballistic phonons generated within one MFP of the surface. They compared this BTE based thermal resistance to the diffusion solution that does not account for the resistance [35–

37]. To address the interfacial resistance they suggest an explicit BTE formulation to include the interface which results in the temperature drop.

The general form of the phonon BTE is written as [38]

$$\frac{\partial D}{\partial t} + v.\nabla_x D = \left(\frac{\partial D}{\partial t}\right)_{scatt} + \dot{q} \qquad 2.16$$

where D represents the phonon distribution function, v represents the phonon group velocity based on dispersion relationship, x is the spatial coordinate and $\dot{q}$ is energy generation rate. The phonon distribution function D is based on three independent variables (one-dimension), time, position and wave vector components. The scattering term depicts changes in particle distribution function from particle collisions with phonons, isotopes, electrons, imperfections, grain boundaries and device boundaries[39–41]. However BTE treats the electrons and phonons as classical particles calculating scattering rates assuming the system to be only slightly deviating from equilibrium. We use the Lattice Boltzmann method which was originally developed for use in the fluid mechanics area but currently is an indispensable tool for solving problems in phonon heat transfer[32,40,42,43]. This technique uses a section of cells on a cellular automata grid[44]. The state of the cells evolve over a number of discrete steps based on the energy state of the neighboring cells. LBM assumes that phonon scattering occurs only at the lattice points while the regime in between is assigned ballistic transport. The time step for measurements are taken to be smaller than the relaxation time of the phonons.

Using the finite difference scheme we obtain the LBM equation as

$$e_i(x + v_i\Delta t, t + \Delta t = e_i\left(1 - \acute{\Gamma}_i\right)e_i(x,t) + \acute{\Gamma}_i e_i^0(x,t) + q'''\Delta t \quad 2.17$$

where e represents the non-equilibrium phonon energy in the direction i and $\acute{\Gamma}$ is the phonon scattering weight factor. The final iteration calculates the equilibrium energy and temperature as

$$e^0 = C\left(T - T_{ref}\right) = \sum e_i w_i \quad 2.18$$

2.3.2.2 Simulation Parameters and Results

In this work, gray one-dimensional BTE simulations are performed assuming a single phonon MFP of 100nm. The simulation domain is 3μm and an average group velocity of $\bar{v}$ = 3344.7 m/s. With heat flux applied in the [1 0 0] direction the temperature rise at the surface and subsequent decay in the system is measured every 1000 timesteps. Figure 2.11 shows a clear transition from the diffusive to the ballistic regime as the thermal penetration depth decreases below 100nm. The simulation data points are fitted with the Fourier's curve for the calculated apparent thermal conductivity. While figure 2.11.a, 2.11.b and 2.11.c show that the MFBTE data shows good agreement with the Fourier's curve, the fitting in 2.11.d does not match. This is because the thermal penetration depth of the system is under 100nm and the phonons are unable to reach k_{Bulk}. The ballistic thermal transport occurring for MF 16GHz results in a non-physical prediction of k for the system – higher than k_{Bulk}.

a)

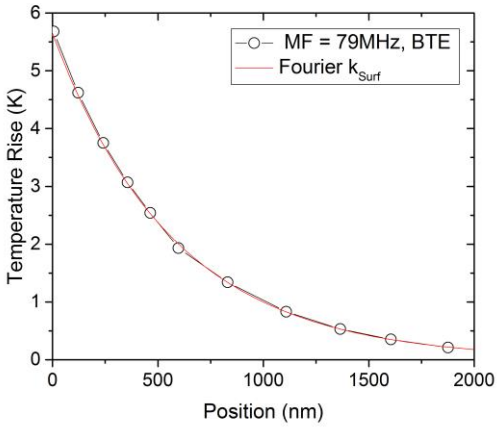

b)

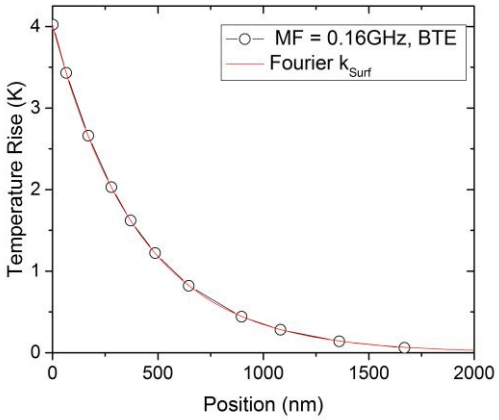

c)

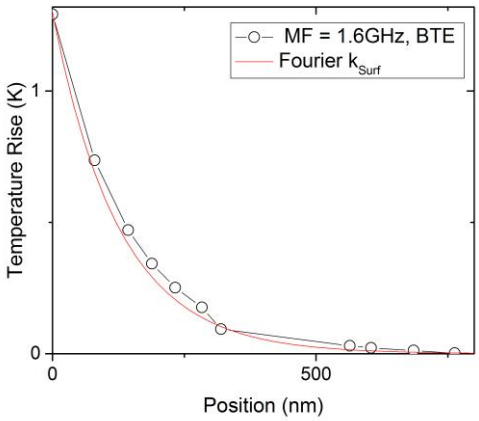

d)

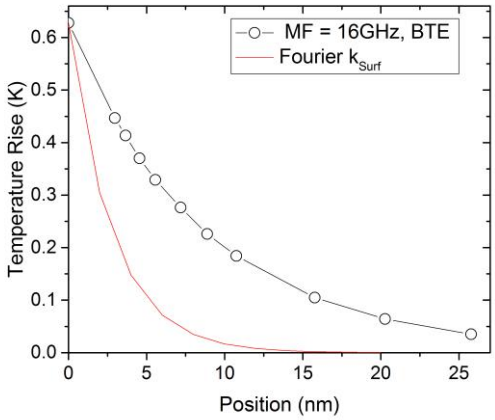

Figure 2.11. MFBTE temperature decay for MF a)79MHz b)0.16GHz c)1.6GHz d)16GHz fitted with Fourier's k_{Bulk}.

2.3.3 Comparison between the Techniques

To analyze phonon contribution to thermal conductivity we compare the results obtained from the three techniques- $MFMD_{Surf}$, $MFMD_{int}$ temperature fitting and $MFBTE_{Surf}$. Figure 2.12.a depicts the normalized thermal conductivity fitted against the penetration depth of the phonons. The figure depicts that the $MFBTE_{Surf}$ calculations retrieve the bulk thermal conductivity value quickly at about 200nm while the $MFMD_{Surf}$ fails to retrieve the thermal conductivity value from the single surface temperature rise value even at 600nm. In contrast the MFMDint temperature points retrieve the bulk thermal conductivity at about 500nm. The $MFMD_{int}$ may be considered as a superior method to retrieve the thermal conductivity values as compared to the $MFMD_{surf}$ on account of utilizing more temperature data points. The $MFMD_{int}$ uses 6-10 data points as compared to the one data point used by $MFMD_{surf}$. This is also fitted with the phonon MFP contribution as calculated from the SED calculations. The trend agrees to some extent with the MDsurf and MDint but underpredicts the value due to isotropic assumption[32].In a similar manner, Figure 2.12.b depicts the thermal conductivity accumulation fitted against the angular frequency of the input heat flux.

Figure 2.12.c is plotted for a constant input heat flux at MF 1 THz. This is then fitted to the analytical solution to Fourier's law using Equation (2.7). The black curve denoting the k_{Bulk} fitting exhibits a lower surface temperature as compared to the values measure via simulation. This is a signature of ballistic transport at the give MF. As a result of this the thermal conductivity predicted is also lower than the bulk value.

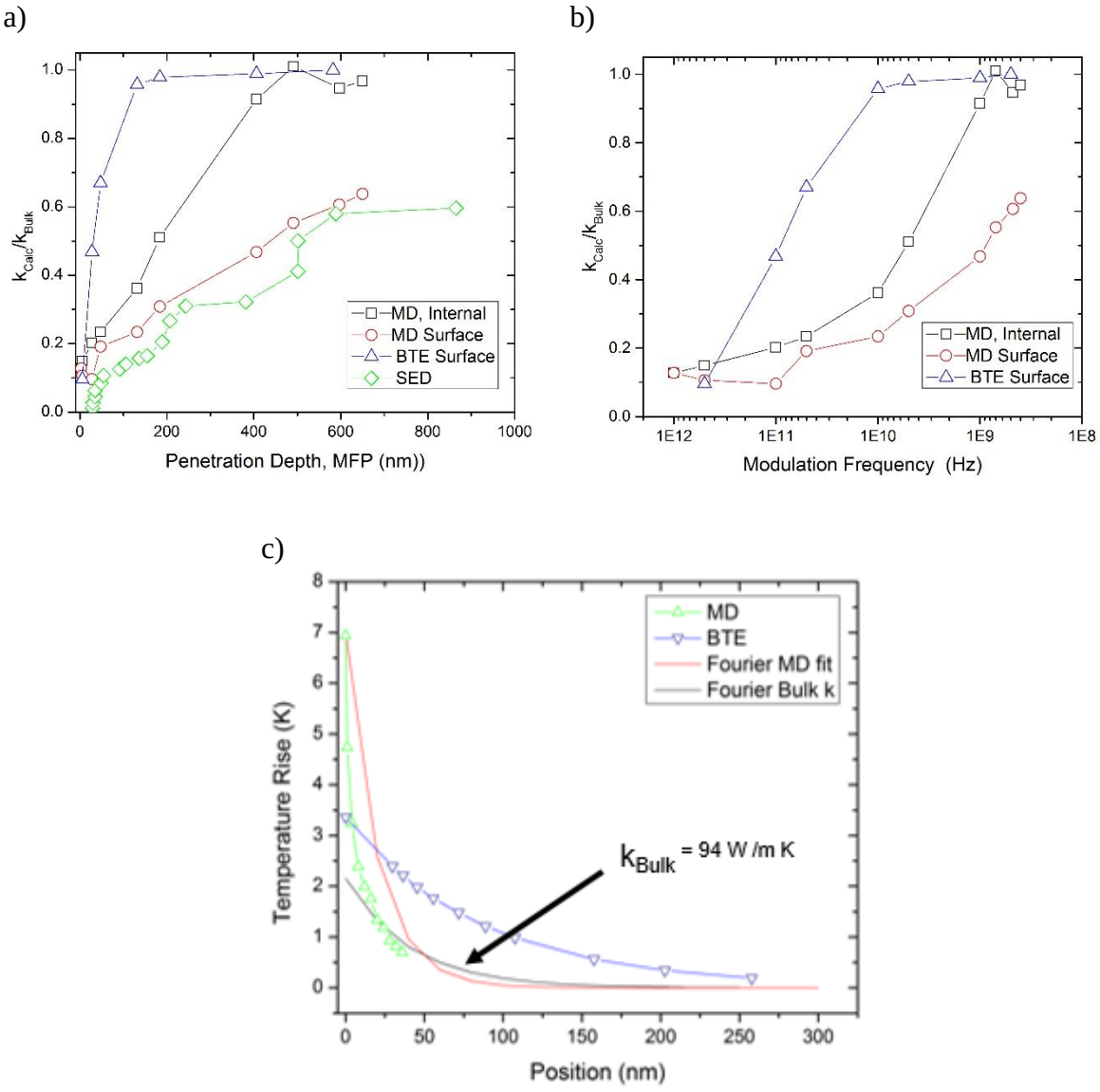

Figure 2.12. a) Comparing accumulating normalized k forMFMDSurf, MFMDInt, MFBTESurf and the SED based MFP against L_p b) Comparing accumulating normalized k against the MF c) Comparing the temperature decay patterens observed in MFMD and MFBTE for a constant heat flux – MF 0.16THz.

2.3.4 Conclusions

A new methodology to measure frequency dependent thermal conductivity is developed using MD. MFMD mimics the current experimentally procedures by predicting the apparent thermal conductivity using the surface temperature of the substrate and further can validate the trend by fitting the temperature profile inside the substrate. MFMD also successfully studies the effect of ballistic transport in the system and is capable of computing the k accumulation curve. These results are to a point validated via gray one dimensional MFBTE simulations which accurately predict the k accumulation via the surface temperature rise but in our case fail while fitting the temperature profile inside at surface for penetration depths less than the considered MFP of the phonon.

$MFMD_{Int}$ and $MFBTE_{Surf}$ give similar K_{Bulk} values but achieve so at different applied modulation frequencies. At the same time the $MFMD_{Surf}$ fails to achieve the k_{Bulk} with the same modulation frequencies.

$MFMD_{Int}$ is spectral in nature and relies on several data points to predict k and thus is considered the most reliable method amongst the three techniques demonstrated.

CHAPTER 3. METAL – NON-METAL INTERFACIAL HEAT TRANSFER

3.1 Metal - Non-Metal Interactions at the Sub-Micron level

3.1.1 Introduction

Thermal properties of nano-composite materials are of great interest because of their application in devices for microelectromechanical systems, data storage, protective coatings, etc. Properties of the composites mainly depend on the size, shape, volume fraction, orientation, interaction of the inclusions and interface effect. In the micro-nano scale domain the heat transfer across interfaces may end up dominating the thermal transport[45,46]. There has been wide variety of research ranging from diamond reinforced metal-matrix composites to improve thermal conductivity[47,48], to study the effect of the shape of the inclusion on the effective thermal properties of the system. As electrons act as the dominant carriers in metals, heat transfer for a metal-non-metal interface occurs by energy transfer between electrons and phonons. The two possible pathways discussed for this exchange are

1. Electrons and phonons coupling through anharmonic interactions at the interface
2. Coupling of phonons of the non-metal with the phonons of the metal and subsequent coupling of phonons with the electrons within the metal.

The anharmonic interactions in the first case can arise due to three major factor,

i) changes of metal electronic potential at the interface,

ii) ion vibrations resulting in oscillations on the metal surface charge or

iii) joint surface modes that result in heat exchange with bulk modes amongst the materials. The second pathway is discussed by Majumdar and Reddy [51]which helps understand that how counter intuitively small is not always good. They use an approximate approach to study the non-equilibrium between electrons and phonons. They assume that electron-phonon energy transfer at the interface is negligible to arrive at the result

$$h = \frac{\sqrt{Gk_p}}{\left[1 + \frac{\sqrt{Gk_p}}{h_{pp}}\right]} = \frac{h_{ep}h_{pp}}{h_{ep} + h_{pp}} \qquad 3.1$$

where h is the interfacial conductance, G is the electron to phonon energy transfer per unit volume, k_e and k_p represent the electron and phonon thermal conductivities and h_{pp} and h_{ep} are the phonon-phonon and electron-phonon conductance respectively.

The effective medium theory was devised to be able to predict an approximate thermal conductivity value for composite materials as a whole. Minnich and Chen modified the approximation to account for inclusions with characteristic length on the order of phonon mean free paths, taking into account the thermal boundary resistance between phases and interface scattering. They compared the monte carlo and BTE simulations with the results from the modified effective medium approximation. They found close agreement for the small particle sizes that they consider [3].

The modified effective medium theory as proposed by Minnich and Chen considers the density of nanoparticles as $1/n^3$ for a spherical nano-particle of diameter, d less than the phonon MFP. To account for the interface scattering and be able to predict the effective

thermal conductivity they considered the interface density -- surface area of the nano-particles per unit volume of composite. The interface density of the particles defined as

$$\rho_{int} = \frac{4\pi d^2}{a^3 4} \qquad 3.2$$

Where ρ_{int} is the interface density for spherical particle and a is the effective cell length. They further consider that if a phonon travels a distance L in the system then with the cross sectional area of the spherical particle acting as the effective collision area, it will encounter $\pi d^2 Ln/4$. This results in a collision mean free path of the phonons as $\lambda_{coll}=4a^3/\pi d^2$.

Based on the Mattheissen's rule the effective MFP of the particles in the host phase are

$$\lambda_{eff}^{-1} = \lambda_{bulk}^{-1} + \lambda_{coll}^{-1} \qquad 3.3$$

where the inverse sum of the bulk and collision MFP give the effective mean free path in the composite material.

This work was then extended by Miranda et al. where they developed the model for spherical inclusions in a nano-composite material[45,46,49]. They compared the predictions of their modified theory and compare the results with BTE simulations to conclude that the size and shape of the particle shows up through the collision cross section per unit volume and mean free path of the energy carriers within the inclusions.

The effective medium theory including Maxwell's scheme amounts to the following Equation (3.4)

$$k_c = (\frac{k_m\left[\left(2k + k_d^{eff} + 2\left(k_d^{eff} - k_m\right)\right]V_d\right)}{2k_m + k_d^{eff} - \left(k_d^{eff} - k_m\right)} \qquad 3.4$$

where k_c is the conductivity of the composite, k_{deff} is the size dependent thermal conductivity of the inclusion, k_m is the thermal conductivity of the matrix material and V_d

represents the volume fraction. For a particle of diameter d the effective thermal conductivity of the composite may be calculated as

$$k_d^{eff} = k_d^{in}/(1 + \frac{2k_d^{in}}{d\ h}) \quad 3.5$$

with h representing the interface thermal conductance.

3.1.2 Two Temperature Model (TTM)

For the case of indirect exchange of energy between the electron and the phonons, the two temperature model of heat conduction is considered as a reliable method to predict their interactions. This is inferred from close agreement with experimental data for electron phonon non equilibrium temperature data[45,52]. The trend of the electron and phonon temperature in the materials can be inferred by taking into account their interactions via the following equations

$$\frac{d^2T_e}{dx^2} - \frac{G}{k_e}(T_E - T_P) = 0 \quad 3.6$$

$$\frac{d^2T_p}{dx^2} + \frac{G}{k_e}(T_E - T_P) = 0 \quad 3.7$$

where T_e and T_p representing the temperatures of the electron and phonons respectively, k_e and k_p are the thermal conductivities for the electron and phonon and G represents the electron phonon coupling factor. Solving these equations for the temperature difference between the electron and phonon we can arrive at

$$T_e(x) = A + Bx + \frac{k_a}{k_e}[C\sinh\left(\frac{x}{d}\right) + D\cosh\left(\frac{x}{d}\right)] \quad 3.8$$

$$T_p(x) = A + Bx + \frac{k_a}{k_p}\left[C \sinh\left(\frac{x}{d}\right) + D \cosh\left(\frac{x}{d}\right)\right] \quad 3.9$$

where k_a is the half of the harmonic mean of the electron-phonon thermal conductivity, d is the intrinsic electron-phonon coupling length, A, B, C and D are the boundary condition dependent constants and x represents the position in the material from the defined origin. The two temperature model does have its limits, being more accurate for material lengths greater than the MFP of the phonons. This was predicted by Qiu and Tien [53]. However electron mean free paths are of the order of a few nanometers, thus taking into consideration the interfacial phonon thermal resistance. This model can be applied for regions as small as a few nanometers.

Yang et al. derived the equations for a two layered system to show that the temperature of an electron is always higher than the phonon temperature in a metal layer. The electron phonon temperature difference also increases linearly with position, but becomes independent of coupling length if the conduction is in the conduction is ballistic.

3.2 Numerical Results

3.2.1 Comparing the EMA models

In this section we analyze the effect of the modified effective medium theory as developed by Chen et al. on the trend of metal inclusion in a silicon matrix. We will designate this as EMA1. We compare this approach with the direct inclusion of the interfacial thermal

conductance into the scheme of Maxwell. We will designate this approach as EMA2. By keeping the volume fraction the same, we increase the size of the inclusions to see the effective thermal conductivity of the composite material. Matrix bulk thermal conductivity of 150 W/mK for Si. We consider a Cu particle with a varying diameter in the matrix, and compare this for two volume fractions – 0.33 and 0.66. Further the effective thermal condu intrinsic thermal conductivities of Cu, Al, Sn and Pb are taken as 401 W/mK, 237 W/mK, 67 W/mK and 35 W/mK [8,54]. Assuming a 5% contribution by the phonons in the bulk thermal conductivity we assign the rest of the thermal conductivity contribution to the electrons. Taking the electron phonon coupling constant to be 10^{17} [51] and electron specific heat as 10^{4} we calculate the interfacial thermal conductance using Equation (3.1). With an assumed constant volume fraction of 0.67 we calculate the effective thermal conductivity of the spherical particle inclusion and fit it to obtain the effective composite thermal conductivity as a function of the particle radius. The comparison for EMA1 and EMA2 in figure 3.1.a shows that the EMA1 shows a lower thermal conductivity at smaller particle sizes. This is due to the fact that the effective thermal conductivity for the particles and host is lower in EMA1 due to inclusion of collision induced MFP. In figure 3.1.b, a trend for the four metals in depicted carrying as a function of their radius. As expected at lower particles radii the thermal boundary resistance counteracts the materials property to aid thermal conductivity and the inclusions start acting as barriers to heat flow.

a)

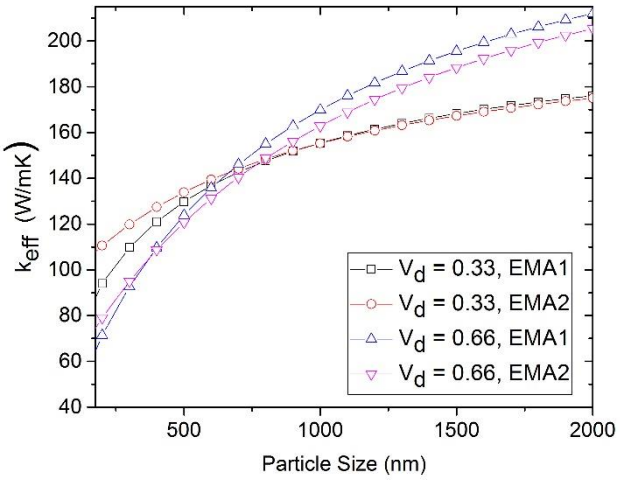

b)

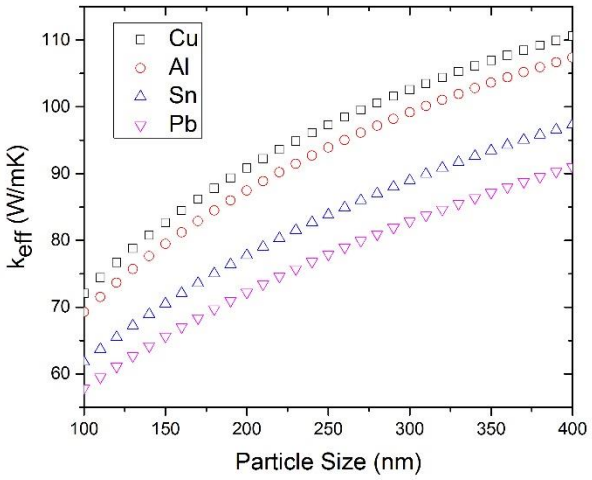

Figure 3.1. a) Comparing the EMA1 and EMA2, showing a trend for particle radius based composite k_{eff}. b) Effective thermal conductivity of particle as a function of particle radius for a constant volume fraction of 0.67. Four metals are considered Cu, Al, Sn and Pn in Si matrix.

3.2.2 FEA Model to Understand Particle Size Effect in Composites

To depict the effect on thermal flow a nano particle may have as compared to a meso-scale particle, in a composite we develop a FEA model. A macro sized model is designed in CATIA V5 as shown in figure 3.2.a to serve as a 40nm diameter copper inclusion, a separate interface resistance layer and a 100nm length Si matrix. The model with the dimensions is depicted in figure3.2.b. A heat flux was applied at the top surface to acquire a temperature gradient of about 1K between the top surface and the bottom surface of the bulk material.

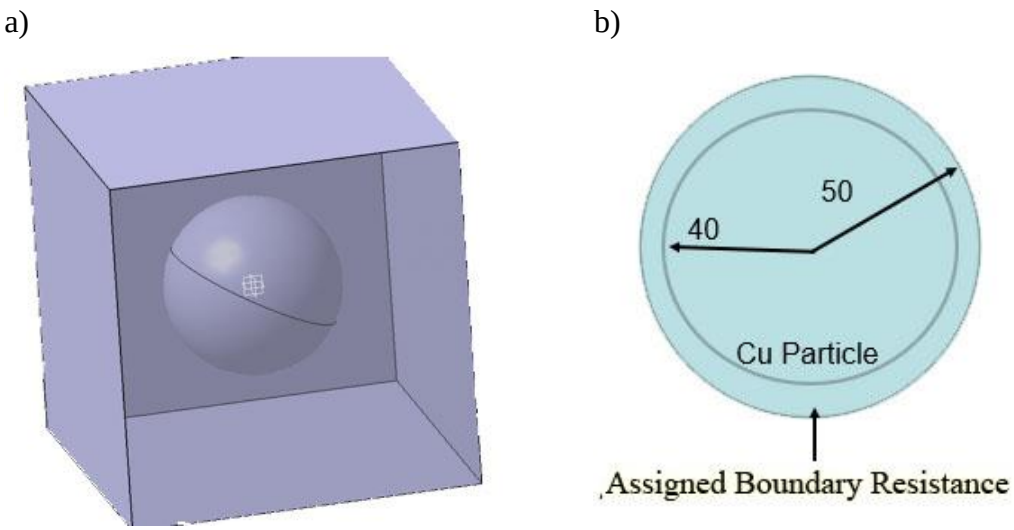

Figure 3.2. a) Catia model to analyze Cu particle in Si matrix b) Dimensions of Cu particle with added interfacial resistance.

The analysis was performed using ANSYS. An unstructured mesh was created with 149837 nodes and 114637 elements. Thermal elements used were SOLID87 which are a 10 node tetrahedral elements. The temperature contour across the ends for the 40 nm Cu inclusion is shown in figure 3.3.a. To validate this the same model is fitted to the two temperature model to acquire temperature drop data across the inclusion interface. This is shown in

figure 3.3.b. The two temperature model validates the values of the temperature drop across the interface.

a) b)

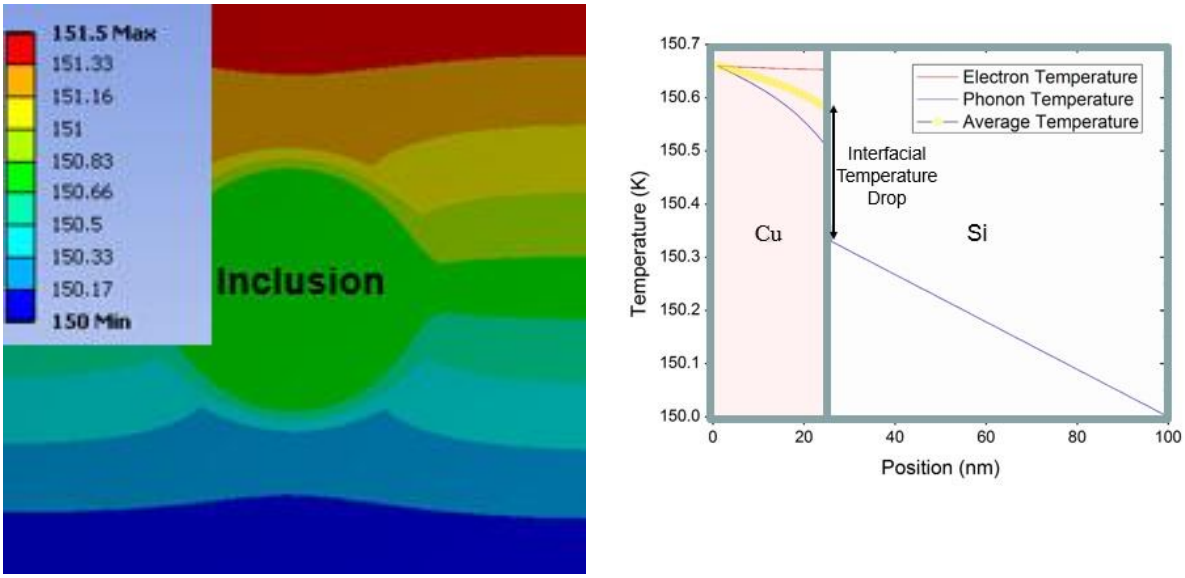

Figure 3.3. a) ANSYS model for Cu particle in Si, temperature gradient across top and bottom surface b) TTM for temperature drop across interface, considering the drop from the temperature within the particle to the exterior of the interface.

The inclusion is observed to be at a temperature of 150.66 K and the temperature just across the assigned interfacial resistance is 150.33.

To be able to visually understand the size effect of the particles on the heat flow within the system the figure 3.4 shows two cases- 3.4.a shows the case with a 40μm particle as compared to a 40nm particle in 3.4.b. The thermal boundary resistance does not come into effect prominently in the first case with the heat flux preferring to flow through the Cu particle. This system overall is more thermally conductive than the bulk matrix alone. In contrast, the second case shows that the particle acts like a heat barrier. The heat flux is

mostly flowing from outside the particle. The interface boundary resistance dominates in this case and the effective thermal conductivity of the system decreases.

a) b)

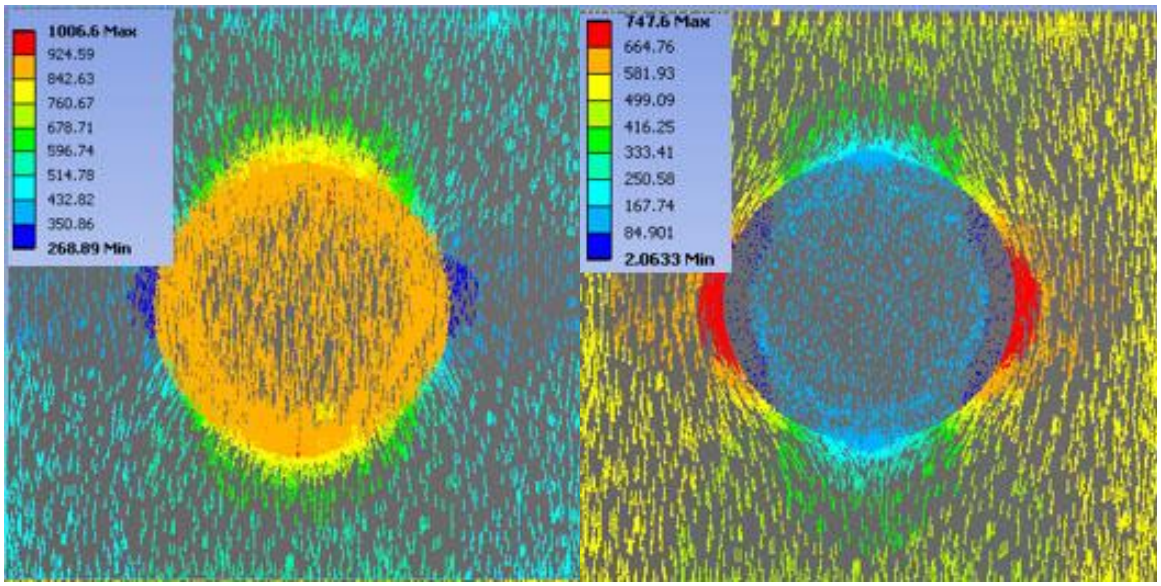

Figure 3.4. a) 40μm particle in Si bulk material having a tendency to absorb heat, b) 40nm particle in Si bulk material acting as a thermal insulator because of the interfacial resistance.

This analysis makes us wonder about the possibility of a dimension of the particle at which the effective thermal conductivity of the composite would remain unaffected, thereby cloaking the particle. Solving by modifying the Equation (3.5)

$$R_{critical} = \frac{\left(\frac{k_{intrinsic}}{h}\right)}{\frac{k_{intrinsic}}{k_{bulk}} - 1} \qquad 3.10$$

Tanking a sample case for copper in silicon, in Equation (3.5) we back substituting effective thermal conductivity of the particle equal to that of the bulk material. We obtain a particle dimension of 766.8nm.

Such parameters may be crucial for applications where modifying the materials composition has no effect on the thermal conductivity but may end up having desirable improvements in the mechanical properties. To test the validity of this size criteria we performed another ANSYS simulation as depicted in figure 3.5.b changing the thermal boundary resistance criteria for the system. As observed in the second case, no significant change in the temperature field is observed signifying no overall change in the flux field in the system.

a) b)

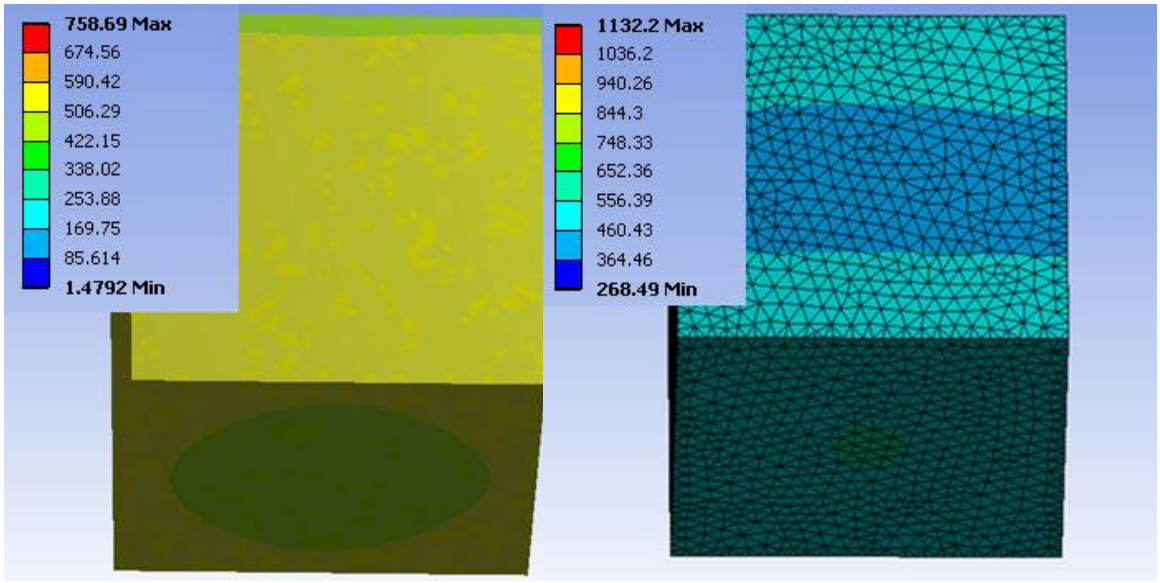

Figure 3.5. a) System with a 40μm particle showing a higher temperature magnitude in the portion directly below the particle, b) System with particle of size $R_{critical}$ showing a constant temperature profile at the bottom surface.

3.3 Conclusions

EMA is directly fitted with interfacial thermal boundary resistance as developed by Majumdar and a trend a particle thermal behavior has been demonstrated. Chen and Minnich's modified effective medium approximation was compared with the direct fitting – EMA1 and EMA2 to demonstrate how the two models deviate at small sizes. EMA1 was found to be more effective for smaller particle sizes as it more accurately takes into account the reduction in effective thermal conductivities of both the host and inclusions. Whereas for larger particle diameters the two approaches converge.

A FEA model was demonstrated with the addition of an external interfacial boundary resistance. This was further used for calculation of critical size of a particle such that the effective thermal conductivity of the inclusion+interface would equal that of the bulk material. It is inferred that at the lower realms of the nano domain a more thorough understanding of the interacting materials is required before designing structures and devices.

CHAPTER 4. DISCUSSIONS

This study helps further understand the MFP contribution of phonons to thermal conductivity in materials by developing a new tool MFMD. The transient MD was used to study thermal transport in both the ballistic and the diffusive region. This tool may be used to calculate the bulk thermal conductivity of materials. In contrast to experiments, the analysis here is not just limited to the temperature rise at the surface of the sample but probes into the temperature profile within the device. The results allow us to conclude that due to the resistance between the heat bath and the interior of the device, it may be of interest to measure experimentally the trend k exhibits based on the temperature profile within the system.

The trend for thermal behavior as a function of size of the inclusions was demonstrated. It was shown that particle sizes may be varied to the effect that they have no effect on the thermal properties of the materials. This aspect may be beneficial for applications where in additives of a certain shape and size may help improve the mechanical properties while not altering the overall thermal behavior of the structure.

LIST OF REFERENCES

LIST OF REFERENCES

[1] G. Pernot, M. Stoffel, I. Savic, F. Pezzoli, P. Chen, G. Savelli, A. Jacquot, J. Schumann, U. Denker, I. Mönch, C. Deneke, O. G. Schmidt, J. M. Rampnoux, S. Wang, M. Plissonnier, A. Rastelli, S. Dilhaire, and N. Mingo, Nat. Mater. **9**, 491 (2010).

[2] D. G. Cahill, P. V. Braun, G. Chen, D. R. Clarke, S. Fan, K. E. Goodson, P. Keblinski, W. P. King, G. D. Mahan, A. Majumdar, H. J. Maris, S. R. Phillpot, E. Pop, and L. Shi, Appl. Phys. Rev. **1**, 011305 (2014).

[3] A. Minnich and G. Chen, Appl. Phys. Lett. **91**, 073105 (2007).

[4] R. B. Wilson and D. G. Cahill, Nat. Commun. **5**, 5075 (2014).

[5] G. Chen, Phys. Rev. B **57**, 14958 (1998).

[6] H. Tian, Z. Tan, C. Wu, X. Wang, M. A. Mohammad, D. Xie, Y. Yang, J. Wang, L.-J. Li, J. Xu, and T.-L. Ren, Sci. Rep. **4**, 5951 (2014).

[7] M. Kaviany, *Heat Transfer Physics* (Cambridge University Press, Cambridge, UK, 2008).

[8] F. P. Incropera, *Fundamentals of Heat and Mass Transfer* (John Wiley & Sons, 2011), p. 1048.

[9] Y. K. Koh, D. G. Cahill, and B. Sun, **205412**, 1 (2014).

[10] G. Chen, Oxford Univ. Press (2005).

[11] C. H. K. Walter G. Vincenti, *Introduction to Physical Gas Dynamics* (1967).

[12] J. P. Freedman, J. H. Leach, E. a Preble, Z. Sitar, R. F. Davis, and J. a Malen, Sci. Rep. **3**, 2963 (2013).

[13] G. C. C. Dames, *Thermal Conductivity of Nanostructures Thermoelectric Materials. In : Thermoelectrics Handbook: Macro to Nano., Edited by Rowe D. M.* (CRC Pres,, Boca Raton, USA, 2006).

[14] Y. Koh and D. Cahill, Phys. Rev. B **76**, 075207 (2007).

[15] K. T. Regner, D. P. Sellan, Z. Su, C. H. Amon, A. J. H. McGaughey, and J. a Malen, Nat. Commun. **4**, 1640 (2013).

[16] D. G. Cahill, Rev. Sci. Instrum. **75**, 5119 (2004).

[17] C. A. Paddock and G. L. Eesley, J. Appl. Phys. **60**, 285 (1986).

[18] A. J. Minnich, J. A. Johnson, a. J. Schmidt, K. Esfarjani, M. S. Dresselhaus, K. a. Nelson, and G. Chen, Phys. Rev. Lett. **107**, 095901 (2011).

[19] F. Yang and C. Dames, Phys. Rev. B **87**, 035437 (2013).

[20] M. P. Allen and D. J. Tildesley, *Computer Simulation of Liquids*, Clarendon, Oxford, (1987).

[21] S. Volz, J. . Saulnier, G. Chen, and P. Beauchamp, Microelectronics J. **31**, 815 (2000).

[22] Y. Wang, A. K. Vallabhaneni, B. Qiu, and X. Ruan, Nanoscale Microscale Thermophys. Eng. **18**, 155 (2014).

[23] P. K. Schelling, S. R. Phillpot, and P. Keblinski, Phys. Rev. B **65**, 144306 (2002).

[24] E. Landry, M. Hussein, and A. McGaughey, Phys. Rev. B **77**, 184302 (2008).

[25] D. A. McQuarrie, *Statistical Mechanics* (University Science Books, Sausalito, 2000), pp. 520–521.

[26] B. Qiu and X. Ruan, arXiv (2011).

[27] A. S. H. and G. Chen, J. Comput. Theor. Nanosci. **Vol. 5**, 1 (2008).

[28] Y. Wang, H. Huang, and X. Ruan, Phys. Rev. B **90**, 165406 (2014).

[29] A. J. H. McGaughey and M. Kaviany, Int. J. Heat Mass Transf. **47**, 1783 (2004).

[30] Y. Wang, B. Qiu, A. J. H. McGaughey, X. Ruan, and X. Xu, J. Heat Transfer **135**, 091102 (2013).

[31] B. Qiu, H. Bao, G. Zhang, Y. Wu, and X. Ruan, Comput. Mater. Sci. **53**, 278 (2012).

[32] J. E. Turney, E. S. Landry, a. J. H. McGaughey, and C. H. Amon, Phys. Rev. B - Condens. Matter Mater. Phys. **79**, 1 (2009).

[33] J. D. Gale, J. Chem. Soc. Faraday Trans. **93**, 629 (1997).

[34] D. G. Cahill, W. K. Ford, K. E. Goodson, G. D. Mahan, A. Majumdar, H. J. Maris, R. Merlin, and S. R. Phillpot, J. Appl. Phys. **93**, 793 (2003).

[35] K. T. Regner, A. J. H. McGaughey, and J. A. Malen, Phys. Rev. B **90**, 064302 (2014).

[36] G. Chen, J. Heat Transfer **118**, 539 (1996).

[37] D. P. Sellan, J. E. Turney, A. J. H. McGaughey, and C. H. Amon, J. Appl. Phys. **108**, 113524 (2010).

[38] A. P. Christensen, Multiscale Modeling of Thermal Transport in Gallium Nitride Microelectronics., 2009.

[39] T. Wang and J. Y. Murthy, Heat Transf. Vol. 3 **2006**, 463 (2006).

[40] F. N. Donmezer, D. Singh, W. James, A. Christensen, S. Graham, and J. Y. Murthy, in *Vol. 10 Heat Mass Transp. Process. Parts A B* (ASME, 2011), pp. 333–343.

[41] N. S. Dhillon and W. Lafayette, (n.d.).

[42] R. Escobar, B. Smith, and C. Amon, J. Electron. Packag. **128**, 115 (2006).

[43] R. A. Escobar and C. H. Amon, J. Heat Transfer **130**, 092402 (2008).

[44] U. Frisch, B. Hasslacher, and Y. Pomeau, Phys. Rev. Lett. **56**, 1505 (1986).

[45] J. Ordonez-Miranda, J. J. Alvarado-Gil, and R. Yang, J. Appl. Phys. **109**, 094310 (2011).

[46] J. Ordonez-Miranda, R. Yang, and J. J. Alvarado-Gil, J. Appl. Phys. **111**, 044319 (2012).

[47] E. A. Ekimov, N. V. Suetin, A. F. Popovich, and V. G. Ralchenko, Diam. Relat. Mater. **17**, 838 (2008).

[48] K. Chu, C. Jia, X. Liang, H. Chen, W. Gao, and H. Guo, Mater. Des. **30**, 4311 (2009).

[49] J. Ordonez-Miranda, R. Yang, and J. J. Alvarado-Gil, Appl. Phys. Lett. **98**, 3 (2011).

[50] K. M. F. Shahil and A. a Balandin, Nano Lett. **12**, 861 (2012).

[51] A. Majumdar and P. Reddy, Appl. Phys. Lett. **84**, 4768 (2004).

[52] J. Fujimoto, J. Liu, E. Ippen, and N. Bloembergen, Phys. Rev. Lett. **53**, 1837 (1984).

[53] T. Q. Qiu and C. L. Tien, J. Heat Transfer **115**, 835 (1993).

[54] D. Singh, J. Y. Murthy, and T. S. Fisher, J. Heat Transfer **133**, 122401 (2011).

APPENDIX

APPENDIX

Table 1. Modulation frequency input heat flux dependent thermal conductivity.

MF 'rad/s'	**Penetration Depth (Fourier) 'nm'**	**K 'w/m.K' $MFBTE_{Surf}$**	**K 'w/m.K' $MFBTE_{Int}$**	**K 'w/m.K' $MFMD_{Surf}$**	**K 'w/m.K' $MFMD_{Int}$**
5e8	597	94	90	57.81951541	89.7232
7e8	491	94	90	52.77064259	95.4689
1e9	406	93.24	90	44.75640795	86.4153
5e9	184	92	90	29.57886552	48.2331
1e10	131	90.455	90	22.78286614	34.4599
5e10	47	63.54	184	18.44417012	22.8518
1e11	27	43	211	9.944972876	22.7898
5e11	5	8.49	1000	11	19.5
1e12	2.7		1600	10	12.2654

VITA

VITA

Academic Particulars

Master of Science, Mechanical Engineering (**May 2015**)

Purdue University, West Lafayette

Bachelor of Technology, Mechanical Engineering (May 2013)

Vellore Institute of Technology, Vellore, India

Work Experience

Birck Nanotechnology Centre, Purdue University, U.S.A. (June - July 2012)

- MPCVD growth of Boron Nitrogen doped few layered Graphene to improve thermal stability from 500K to 1200K
- Oxidation testing for doped graphene coating on copper substrate

Ecole Polytechnic de l'universite de Tours, France (May to July 2011)

- High Temperature Tribology of Carbon nanotubes reinforced Alumina Titania Coatings on Titanium Alloys – improvement of surface hardness and wear resistance
- Training in Scanning Electron Microscopy

LIST OF PUBLICATIONS

LIST OF PUBLICATIONS

Tribological and Corrosion Study of Carbon Nanotubes Reinforced Alumina 13Titania Coating on a Ti13Nb13Zr Substrate

E. Mathew, Shivi Singh, S. T. Aruna, G. Manivasagam, R. Caroline, N. Ranganathan page number 407-416, Surface Modification technologies Volume 26, ISBN 978-81-926196-0-6

CNT Reinforced Alumina Coating on Grey Cast Iron- A Tribological Study
Shivi Singh, Eshaan Mathew, Sagar Anand, Geetha Manivasagam and R. Asokamani, Advances in Applied Surface Engineering, June 2011, 978-981-08-7922-8

Conference Publications:

National Conference on Challenges in Biomedical Research in VIT, Vellore December 23rd to 24th 2013 (**Best Poster presentation Award**, by co-author: Tribological and corrosion behaviors of Warm and Hot rolled Ti-13Nb-13Zr Alloys in Simulated Body Fluid Conditions)

ICYRAM-2012 International Conference of Young Researchers on Advanced Materials in Singapore July 1th to 6th (Poster presentation by co-author: Nano nickel as anode catalysis for direct borohydride (DBFC) and alkaline (AFC) fuel cell)

SMT 26-2012 International Conference on Surface Modification Technologies in Lyon, France June 20th to 22nd (Paper presentation by co-author: Tribological and corrosion study of carbon nanotubes reinforced alumina 13 titania coating on a Ti13Nb13Zr substrate)

SET-2012 4th International Conference on "Science, Engineering and Technology" in VIT, Vellore May 3rd to 4th

(**Best Paper Presentation Award:** Calculation and evaluation of carbon footprint of hurricane thane)

ICHT-2011 International Conference on Harnessing Technology in Oman, Feb 12th to 14th (Paper presentation by co-author:

Comparative study on performance and emission characteristics by biodiesels)

APIC-2010 International Conference on Applied Surface Engineering in Singapore Oct-19th to Oct-22nd (Paper presentation: Carbon nanotubes reinforced Alumina-a potential application for waste heat recovery in automobiles)

Papers in progress

Eshaan Mathew, Yan Wang, and Xiulin Ruan, "An investigation of ballistic-diffusive phonon transport via modulated input flux non-equilibrium molecular dynamics", in preparation

Taekyung Lee, Eshaan Mathew, Santhosh Rajaraman, Geetha Manivasagam, Ashok Kumar Singh, and Chong Soo Lee, "Tribological and Corrosion Behaviors of Warm- and Hot-Rolled Ti-13Nb-13Zr Alloys in Simulated Body Fluid Conditions", International Journal of Nanomedicine, accepted.